

Physico-chemical spectroscopic mapping of the planetary nebula NGC 40 and the 2D_NEb, a new 2D algorithm to study ionised nebulae

M. L. Leal-Ferreira^{1*}, D. R. Gonçalves¹, H. Monteiro^{2,3} and J. W. Richards^{4,5}

¹UFRJ - Observatório do Valongo, Ladeira do Pedro Antônio 43, 20080-090, Rio de Janeiro - RJ, Brazil

²Núcleo de Astrofísica Teórica-CETEC-UNICSUL, Rua Galvão Bueno, 868, 01506-000, São Paulo - SP, Brazil

³Universidade Federal de Itajubá, Av. BPS, 1303, Itajubá - MG, Brazil

⁴Astronomy Department, 601 Campbell Hall, University of California Berkeley, Berkeley, CA 94720, USA

⁵Statistics Department, 367 Evans Hall, University of California Berkeley, Berkeley, CA 94720, USA

Accepted...; in original form...

ABSTRACT

In this paper we present an analysis of the physical and chemical conditions of the planetary nebula NGC 40 through spatially-resolved spectroscopic maps. We also introduce a new algorithm –2D_NEb– based on the well-established IRAF *nebular* package, which was developed to enable the use of the spectroscopic maps to easily estimate the astrophysical quantities of ionised nebulae. The 2D_NEb was benchmarked, and we clearly show that it works properly, since it compares nicely with the IRAF *nebular* software.

Using this software, we derive the maps of several physical parameters of NGC 40. From these maps, we conclude that $T_e[\text{N II}]$ shows only a slight temperature variation from region to region, with its values constrained between $\sim 8,000$ K and $\sim 9,500$ K. Electron densities, on the other hand, have a much more prominent spatial variation, as $N_e[\text{S II}]$ values vary from $\sim 1,000$ cm^{-3} to $\sim 3,000$ cm^{-3} . Maps of the chemical abundances also show significant variations. From the big picture of our work, we strongly suggest that analysis with spatial resolution be mandatory for more complete study of the physical and chemical properties of planetary nebulae.

Key words: atomic data - ISM: abundances - planetary nebulae: individual: NGC 40.

1 INTRODUCTION

Stars of low and intermediate mass ($0.8 - 8 M_{\odot}$) represent 95% of the evolved stars in the Galaxy and, because of the initial mass function, can be important sources of enrichment of He, N and C in the Interstellar Medium (ISM) (e.g., Yin et al. 2010). Although supernovae are expected to be the main source of enrichment for most species (Chiappini, Romano & Matteucci 2003), van den Hoek & Groenewegen (1997) and Marigo (2001) predicted theoretically the possibility that planetary nebulae (PNe) progenitor stars also produce O and Ne and dredge these elements up to the stellar surface, resulting in possible enrichment of the ISM. In any case, PNe and the study of their abundances are clearly important tools to study stellar evolution as well as –by considering elements other than those just discussed– revealing the imprint of

ISM abundances when their progenitor stars were formed, in the Galactic as well as extragalactic context.

The outer layers of the intermediate mass stars, which were enriched throughout their evolution, are ejected during the Asymptotic Giant Branch (AGB) and post-AGB phases, and subsequently ionised by the remnant hot nucleus, referred to as the central star (CS). Analysis of the ionization lines formed in the ejected envelopes of these evolved stars is one of the most important ways in which the chemical and physical characteristics of the gas are studied. However, the great majority of work done in this field utilizes single slit spectroscopy to measure the ionization lines and thus is limited to obtaining average values across the observed region of the slit (or across multiple regions, as it is sometimes done). Utilizing single slits is extremely limiting in the analysis of these objects, especially considering the high complexity of PNe morphology. In single-slit analysis, the possible spatial variations of PNe are usually ignored.

However, spatial variations in the chemical and physical conditions of PNe have been detected in previous works

* Currently at Argelander-Institut für Astronomie, University of Bonn, Auf dem Hügel 71, D-53121 Bonn, Germany. E-mail: ferreira@astro.uni-bonn.de (MLLF)

using long slits. Guerrero et al. (1996), for example, using long-slit spectra, found that the N/O ratio varies from 0.4 to 4.2 from one region to another in the planetary nebula K 4-55. Moreover, also using long-slit spectra, Balick et al. (1994) found N/H abundance gradients in a few PNe. In particular they claimed to have found overabundance factors of 2 for NGC 6826 and NGC 6543 and 5 for NGC 7009, respectively. On the other hand, another empirical study of NGC 7009 (Gonçalves et al. 2003) lowered the overabundance factor to at most 2, and a detailed 3D photoionization modelling of the nebula eliminated completely the need of any overabundance to explain the observed long-slit as well the narrow-band images of the nebula (Gonçalves et al. 2006). By investigating 13 bipolar PNe using long-slit spectrophotometry, Perinotto & Corradi (1998) concluded that (within the errors) He, O, and N abundances are constant throughout the nebulae, and that the Ne, Ar, and S abundances are also constant, but their face values have systematic increases toward the outer regions of the nebulae. The latter was attributed to inaccuracies in the ionization correction factors.

In recent years a new tool for obtaining spectroscopic data has been developed. The Integral Field Unit (IFU) is a tool that utilizes a square array of lenses remapped to a slit and then imaged through a spectrograph to obtain spatially resolved data (Ren & Allington-Smith 2002). Tsamis et al. (2008) were the first to use this tool to investigate the spatial variations of PNe parameters. They verified that there is variation on the discrepancy of the O^{++} abundances obtained from the collisionally excited lines (CEL's) and optical recombination lines (ORL's) on the studied PNe. They established correlations between the ionization state of the gas and the discrepancies of O^{++} for 2 PNe and between the discrepancy of the O^{++} and the abundances of C^{++} and O^{++} with the electron temperature for all 3 studied PNe.

Similar kinds of data can be produced by a spectroscopic mapping technique developed by Monteiro et al. (2004), in which multiple parallel long-slit spectra of a nebula are interpolated to create emission-line maps. Both types of data, those obtained from IFU and those found by the spectroscopic mapping technique, enable better spatially-resolved analysis of ionised nebulae than those based on single long-slit spectra. Spatially-resolved data are also critical in constraining photoionization models which are now fully three-dimensional and can produce a great number of observable quantities, including projected images for each emission line. Photoionization models that utilize these constraints were obtained by Monteiro et al. (2004), Monteiro et al. (2005), Schwarz & Monteiro (2006) for NGC 6369, Menzel 1 and NGC 6781 as well as by Morisset & Georgiev (2009).

To further our understanding of the spatial variations of the physical and chemical properties of PNe, we present in this work results of the study of NGC 40 using spectroscopic mapping. Following the morphological classes of Balick et al. (1987), from their $H\alpha$, [N II] and [O III] images, the PN NGC 40 has an elliptical shape, which can also be seen in the $H\alpha$ narrow band image obtained in our observing run (Figure 1). Two distinct structures are found within the main elliptical region: a bright inner rim and an outer shell. A filament-like structure can also be identified beyond the outer shell, on the northeast region. The [O III] emission,

originating in a hotter, low-density medium, is located between the hot bubble and the $H\alpha$ (or [N II]) filaments, and is better represented by a ring like structure (Balick et al. 1987).

In X-rays NGC 40 also shows a ring-like emission region, and the correspondence of this region with the inner rim indicates that the bright envelope, seen in the optical image, is caused by the shocked CS fast wind. The absence of X-ray emission in the region of an apparent aperture in the inner rim suggests that this wind is quite spherical (Montez et al. 2005). Based on UV data, Clegg et al. (1983) suggest that the C IV 1549 Å emission from the nebular envelope is too strong to have been produced by normal thermal processes, and that it is probable that this emission is a consequence of processes related to the central star wind.

We note that there is a discrepancy in temperature determinations for the CS of NGC 40, a Wolf-Rayet (WC8), in the literature. Feibelman (1999) calls our attention to the peculiarity of the fact that NGC 40 is a low-excitation PN but seems to be excited by a 90,000 K central star. However, a temperature of about 40,000 K, which would be consistent with a low excitation PN, is usually adopted for the NGC 40 central star (Stankevich 1983; Pottasch et al. 2003). Bianchi & Grewing (1987) argue that a “carbon curtain”, located around the CS, could be the mechanism responsible for hiding the CS true effective temperature.

A number of works have dealt with the physical parameters and chemistry of NGC 40 in the past decades (Pottasch et al. 2003; Liu et al. 2004a; Liu et al. 2004b). These authors investigated different regions of the nebula utilizing inconsistent slit configurations or apertures, and thus found results that differ greatly from one paper to another. Even though these works provide a reliable overall picture of the object, they fail to give more detailed information that could potentially lead to important clues as to shaping mechanisms and enrichment patterns, among others.

One important practical limitation in dealing with spatially resolved data is the fact that all currently-available tools used to estimate the physical and chemical properties of PNe have been limited to single numerical values consistent with integrated long-slit fluxes. An alternative to the above could be to implement scripts written for IRAF, which would derive the physical quantities in a pixel per pixel, or region per region fashion, and then to arrange all the results together. However, these kinds of analyses have rarely been reported.

In this work we present a tool, based on the well established IRAF *nebular* package (stdas.analysis; De Robertis, Dufour & Hunt 1987), which is capable of working with two-dimensional data, such as IFU and spectroscopic maps. This tool, the 2D_NEB package, has been tested and shown to be consistent with results obtained with IRAF *nebular* procedures (see Sec. 3.4). We also utilize the 2D_NEB package to study the PN NGC 40 and present the first spatially resolved results of the spectroscopic mapping of this nebula, for which we have obtained the extinction coefficient, electron density and temperature, and ionic abundances of several elements.

This paper is structured as follows. In Section 2 the acquisition and reduction of the data are discussed. Section 3 presents the method of data treatment, including a descrip-

tion of the spectroscopic mapping technique and explanation of those algorithms included in the 2D_NEB package that were developed to analyse spectroscopic maps. Some benchmarks of this new package are also given within Section 3. In Section 4 the empirical results for one of the long-slits observed in this work are compared with those obtained from the spectroscopic maps by means of the 2D_NEB package. Section 5 is dedicated to our spatially resolved results for NGC 40, while the summary and conclusions are in Section 6.

2 DATA ACQUISITION AND REDUCTION

The observational data used in this work includes both an H α image and optical long-slit spectra. The observations were obtained on the night of 2005 October 28th, at the 2.56 m Nordic Optical Telescope (NOT), located at the Observatorio del Roque de los Muchachos (European Northern Observatory, La Palma, Spain). For both the image and spectra, the Andalucia Faint Object Spectrograph and Camera (ALFOSC), which has a pixel scale of 0.189'' pixel⁻¹, was used.

The H α image has an exposure time of 30 s and the seeing during the exposure was 0.89''. In this paper this image is used only for comparison with the H α spectroscopic map that is constructed using the spectra, as described in detail below. The reduction of the H α image included only bias subtraction, in addition to flat-field (dome and sky) correction. No photometric calibration of this image was performed. It is worth noting, however, that the resolution of the H α image is better than the resolution achieved with the maps.

For spectroscopy, the long-slit width used was 1.3''. The ALFOSC was used with the grism number 7, which has 600 rules mm⁻¹ and a spectral coverage from 3850 Å to 6850 Å. The reciprocal dispersion of the binned pixel is 3.0 Å pixel⁻¹. The slit was located on 16 different parallel positions across the nebula. The distance between them was fixed and set at 3''. For 15 of those positions the exposure times were 3 × 300 s. For slit B only one 300 s exposure was taken. Figure 1 shows our NOT H α image, and also the relative slit positions across the nebula. Note, in addition, that the slits do not cover the entire object. Slit lengths in Figure 1 are reduced for visualization purposes with their respective labels used throughout the text.

The data reduction was performed using the standard procedures for long-slit spectroscopy of the Image Reduction Analysis Facility (IRAF). Bias frames, flat-field, helium-neon wavelength calibrations and standard star (G191B2B) exposures were obtained during the observation runs, and used in the reduction/calibration procedure. Three spectra per slit position were taken to improve the signal-to-noise ratio (S/N) and eliminate cosmic rays. The only non-standard procedure used was binning on the dispersion axis. This was necessary to improve the wavelength (λ) calibration due to the fact that the helium-neon lamp was resolved in the arc frames.

The final calibrated spectrum for slit G, which passes through the central star, is shown in Figure 2. Fluxes here are representative of the emission integrated along the slit, which we will later call "WN" (whole nebula) when com-

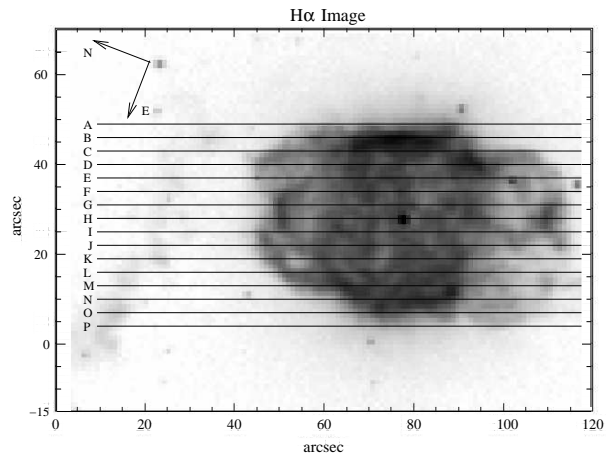


Figure 1. NGC 40 image, observed with an H α filter. The parallel slit positions are represented by lines and labeled by letters.

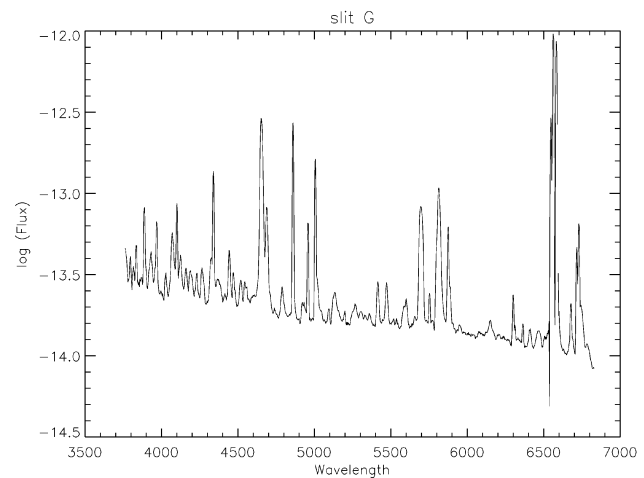


Figure 2. Spectrum of the NGC 40, integrated over the whole slit G.

paring long-slit measurements and results obtained from the spectroscopic maps, in Sections 3.2 and 4.

3 2D OBSERVATIONS AND TOOLS FOR GASEOUS NEBULAE ANALYSIS

3.1 Spectroscopic Mapping Construction

Emission-line mapping is a technique in which the spatial profiles from a set of parallel slits, for a given emission-line, are combined to create an emission-line map of the nebula (Monteiro et al. 2004). We applied this technique using the 16 parallel long-slit spectra described above, to obtain the emission-line maps of NGC 40. These maps correspond to a field of view of 120'' × 47'' (see Figure 3).

This method has been previously applied to Hubble 5, NGC 6369, Mz 1 and NGC 2022 (Rice et al. 2004; Monteiro et al. 2004; Monteiro et al. 2005 and Mateluna-Perez et al. 2006, respectively), providing informative quantities such as the total emitted flux of each ob-

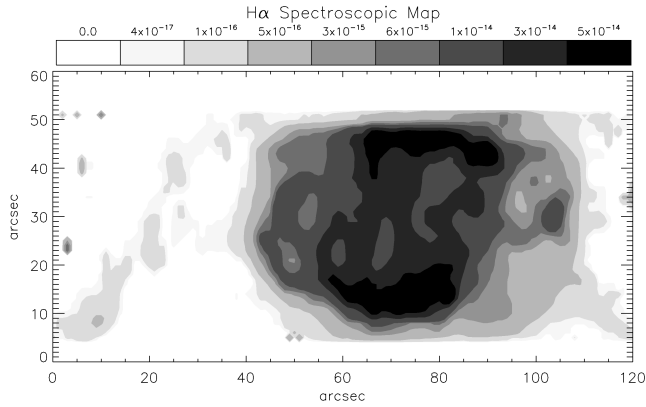


Figure 3. $H\alpha$ spectroscopic map of NGC 40, obtained with the spectroscopic mapping reconstruction technique. Fluxes are given in $\text{erg cm}^{-2} \text{s}^{-1}$.

ject and variations of density and temperature across the nebulae, among others. For example, Monteiro et al. (2005) found indication of the presence of a dense ring and of a bipolar structure of lower density for the planetary nebula Mz 1. Based on that map, they proposed a tridimensional hourglass model to represent the gas distribution of the nebula.

In the present paper, the above method was applied to generate 31 spectroscopic maps of the PN NGC 40, each corresponding to a different emission line. The generated maps were corrected for the effects of field rotation due to the AtI-Azimuth nature of the telescope as well as for differential atmospheric refraction, using the tables of Filippenko (1982). To avoid the presence of pixels with spurious information, all created maps have been submitted to a signal to noise ratio (SNR) cut. These cuts were done by applying a mask in which all the pixels with a SNR lower than a certain value were artificially substituted by 0 (zero). For the brighter emission-lines, the adopted value was SNR equal to 7. On the other hand, this limit did not work for the weaker emission-lines, as almost no signal would survive to the noise-mask cleaning. To handle this problem, noise-masks based on different values were tried. Table 1 presents the list of all the 31 emission-line maps that were constructed, and the correspondent SNR cut-offs (SN_{cut}) of these maps. The third, fourth and fifth columns of this table show, respectively, the integrated spectroscopic map fluxes (F_λ) –corresponding to the emission of the entire observed nebula–, the extinction-corrected intensities (I_λ , as will be discussed in Section 5.1), and the number of the figure in which the map is presented in this paper (Fig.).

Figure 3 shows the $H\alpha$ spectroscopic map. As we noted in Figure 1, the fact that slits do not cover the entire nebula is clearly seen here: the bright edges determine the limits of our observations and correspond to the slits A and P. It is evident from Figure 3 that the $H\alpha$ structures of the image in Figure 1 are well-reproduced by the spectroscopic map. The latter apply not only to the bright elliptical nebular components –the inner rim and outer shells–, but also to the much fainter structures of smaller scales, as well as to the extended filaments.

Table 1. List of the 31 spectroscopic maps with the corresponding SNR cut-offs. Observed fluxes and intensities (extinction-corrected) are normalized to $H\beta = 100$.

Line Identification	SN_{cut}	F_λ	I_λ	Fig.
H10 3797	7.0	3.15	3.98	–
H9 3835	7.0	6.48	7.27	–
H8+He I 3888	7.0	15.40	17.24	–
H ϵ + [Ne III]+He I 3968	7.0	11.38	13.79	–
[S II]+[S II] 4069+76	4.0	0.64	0.73	–
H δ 4101	7.0	18.97	22.43	–
H γ 4340	7.0	38.81	43.85	–
He I 4388	2.5	0.84	0.05	–
He I 4471	7.0	1.75	1.92	–
Mg I 4563+71	3.0	0.15	0.14	–
[C III]+[C IV] 4652	4.0	0.14	0.14	–
He II 4686	2.0	0.02	0.01	–
[Ar IV] 4711	2.5	0.08	0.05	–
H β 4861	7.0	100.00	100.00	5
He I 4921	7.0	1.03	1.01	–
[O III] 4959	7.0	20.38	19.35	–
[O III] 5007	7.0	64.22	58.69	5
[N I] 5198+5200	5.0	0.045	0.41	–
[Cl III] 5517	4.0	0.12	0.10	–
[Cl III] 5537	5.0	0.73	0.43	–
[O I] 5577	5.0	1.01	0.56	–
[N II] 5755	7.0	3.11	2.57	–
He I 5876	7.0	13.61	11.00	–
[O I] 6300	7.0	3.33	2.56	–
[O I] 6363	7.0	0.87	0.67	–
[N II] 6548	7.0	113.54	84.76	–
H α 6563	7.0	400.44	297.23	3
[N II] 6584	7.0	346.77	253.76	5
He I 6678	7.0	3.11	2.28	–
[S II] 6717	7.0	12.41	9.11	–
[S II] 6731	7.0	16.97	12.41	5

Observed $H\beta$ flux, $F(H\beta)$: $1.52 \times 10^{-11} \text{ erg cm}^{-2} \text{ s}^{-1}$.

3.2 Robustness of the 2D flux measurements

To check the accuracy of the technique, what follows is the comparison between the fluxes measured directly from a single slit and those obtained from the spectroscopic map. Several fluxes from the slit G (see Figure 1) were compared with the fluxes measured from the region corresponding to slit G in the maps.

Flux measurements from slit G were obtained using the *splot* task of IRAF. These measurements have been normalized to correspond to a region whose width is 1 arcsec (following the fact that the resolution of the maps is $1'' \text{ pixel}^{-1}$). The comparison is made for 5 separate nebular regions. The extent of each of these regions, at the position of slit G, is given in Table 2.

The emission-lines used for comparison were selected in such a way that isolated, blended, strong and weak lines were each chosen. These measurements are shown in Table 3, together with the relative errors between the two types of flux measurements. In more than 75% of the cases, the discrepancies are lower than 10%. In the worst case, it is 25%.

The observed discrepancies are likely due to effects specific to the regions chosen, such as a single pixel with a discrepant value, since this value will affect the summed flux of the region. Additionally, since the maps are constructed by interpolating between the slits, discrepancies might oc-

Table 3. Comparison between observed fluxes measured from the slit G and from the corresponding region in the emission-lines maps. Fluxes are given in $\text{erg cm}^{-2} \text{s}^{-1}$.

Line Identification	NOS			NIR			SIR		
	slit G	map	δ (%)	slit G	map	δ (%)	slit G	map	δ (%)
H β 4861	3.22(-14)	3.53(-14)	8.8	1.18(-13)	1.39(-13)	14.5	1.37(-13)	1.41(-13)	2.9
[O III] 4959	3.59(-15)	4.50(-15)	20.2	2.80(-14)	2.86(-14)	1.9	3.07(-14)	3.24(-14)	5.2
[O III] 5007	1.10(-14)	1.48(-14)	25.2	8.49(-14)	8.85(-14)	4.0	9.37(-14)	9.97(-14)	6.1
[N II] 6548	3.94(-14)	4.17(-14)	6.5	1.36(-13)	1.60(-13)	14.9	1.53(-13)	1.59(-13)	3.9
H α 6563	1.30(-13)	1.39(-13)	6.2	4.71(-13)	5.47(-13)	13.8	5.45(-13)	5.57(-13)	2.2
[N II] 6584	1.18(-13)	1.25(-13)	5.6	4.13(-13)	4.85(-13)	14.9	4.68(-13)	4.78(-13)	2.0
[S II] 6717	5.10(-15)	5.24(-15)	2.7	1.80(-14)	1.90(-14)	5.2	1.77(-14)	1.68(-14)	5.9
[S II] 6731	6.62(-15)	6.87(-15)	3.6	2.45(-14)	2.82(-14)	13.1	2.50(-14)	2.45(-14)	2.2

Table 3 – continued

Line Identification	SOS			WN		
	slit G	map	δ (%)	slit G	map	δ (%)
H β 4861	3.00(-14)	3.00(-14)	0.0	3.88(-13)	3.89(-13)	0.1
[O III] 4959	1.98(-15)	1.84(-15)	7.5	7.49(-14)	7.13(-14)	5.0
[O III] 5007	5.93(-15)	6.15(-15)	3.5	2.25(-13)	2.21(-13)	1.8
[N II] 6548	3.55(-14)	3.57(-14)	0.6	4.14(-13)	4.22(-13)	1.7
H α 6563	1.20(-13)	1.19(-13)	0.3	1.47(-12)	1.48(-12)	0.4
[N II] 6584	1.08(-13)	1.08(-13)	0.5	1.28(-12)	1.29(-12)	0.6
[S II] 6717	4.67(-15)	4.34(-15)	7.4	5.25(-14)	4.64(-14)	13.1
[S II] 6731	5.58(-15)	5.43(-15)	2.7	8.27(-14)	6.59(-14)	25.4

Table 2. Nebular regions of NGC 40, as defined along slit G.

Region	ID	Approximated extension (arcsec)
North Outer Shell	NOS	from 46 to 57
North Inner Rim	NIR	from 60 to 76
South Inner Rim	SIR	from 79 to 99
South Outer Shell	SOS	from 101 to 112
Integrated nebular emission	WN	from 46 to 112

cur due to the fact that the exact slit position is not extracted from the map. Figure 4 shows a comparison of the spatial profile extracted from the map and that from slit G. In this figure the profiles of [O III] 5007 Å, [N II] 6584 Å, and [S II] 6731 Å emission lines are plotted. The profile of slit G is represented by the solid line, while that of the spectroscopic map is depicted by the dashed one. Note that, with the exception of the central region –where the central star is located–, the correspondence between both profiles (or emission distribution) is very good. It is also evident that the majority of the discrepant regions correspond to either high intensity gradients or low SNR regions, in the spatial axis. This result shows that the spectroscopic mapping technique is, in fact, a reliable method of representing the emission-line fluxes.

3.3 Tools to deal with 2D emission-line maps

To perform the usual diagnostic calculations efficiently for the emission-line maps, it was necessary to develop a number of IDL routines. The set of routines we built compose the 2D_NEb package, which is described in what follows. The

software package is divided in two parts: the first one is responsible for extinction correction and the second calculates the physical and chemical conditions of the nebula (N_e , T_e , ionic and total chemical abundances). The 2D_NEb package was built based on tasks of the IRAF stsdas.analysis *nebular* package, adapted to work with 2D images. As such, all the results generated by these tools are 2D maps created in fits file format.

The routines that compose the first part of the package are based on the Osterbrock & Ferland (2006) formalism, and are responsible for calculating the extinction coefficient, $c(\text{H}\beta)$, and correcting the data for reddening. The Balmer lines are used to determine $c(\text{H}\beta)$. For these tasks the user can choose between H α , H γ or H δ –relative to H β –, and can decide which extinction curve will be adopted: Seaton (1979) or Cardelli, Clayton, & Mathis (1989), with the coefficients reviewed by O’Donnell (1994). When using Cardelli, Clayton & Mathis (1989) curve, it is necessary to assume a value for the R_ν parametrization coefficient, defined as $R_\nu = (A_\nu / E(\text{B-V}))$. The default value of R_ν , used for the calculations hereafter, is 3.1 (Cardelli et al. 1989).

The remaining routines of 2D_NEb were based on the IRAF *temden* task, following the recipes given by De Robertis et al. (1987). These routines are responsible for solving the equation of statistical equilibrium. The atomic data used in our tools are read from IRAF’s atomic data directory. The electron temperature (T_e) and density (N_e) are determined from the solution of the equations of statistical equilibrium. This package also calculates chemical abundances (ionic and total). The latter procedures were based on the *ionic* and *abund* tasks of the IRAF facility. To perform these calculations, the effective recombination coefficient for the H β and the He main transitions, not included

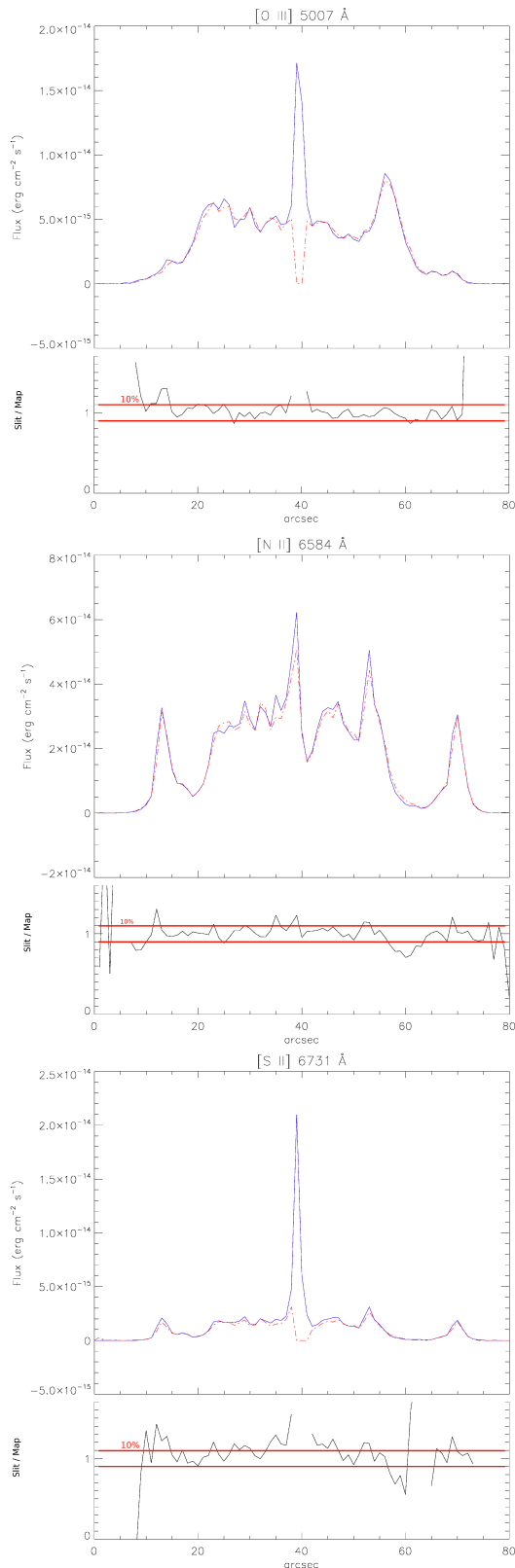


Figure 4. Comparison between the slit and spectroscopic map fluxes (in $\text{erg cm}^{-2} \text{s}^{-1}$). From top to bottom it is shown: [O III] 5007 Å, [N II] 6584 Å, and [S II] 6731 Å. For each emission, the solid line shows the emission measured directly from slit G, and the dashed line shows the emission from the spectroscopic map. In the bottom of each plot it is shown the ratio between both measurements. The region where the difference between the fluxes is lower than 10% is highlighted between 2 horizontal lines.

Table 4. Extinction correction performance.

Line ID (λ in Å)	F	$c(H\beta)$	I_{2d_neb}	$I_{redcorr}$
[O II] 3727	33.4	1.13	77.2	77.2
[O II] 3727	10.1	0.70	17.0	17.0
H γ 4101	14.7	0.26	16.9	16.9
H γ 4101	16.8	0.43	21.1	21.1
[O III] 5007	120.8	0.50	115.7	115.7
[O III] 5007	1220.0	0.33	1185.5	1185.4
[N II] 5755	2.2	1.20	1.3	1.3
[N II] 5755	3.2	0.19	3.0	3.0
[S II] 6731	20.2	0.38	15.3	15.3
[S II] 6731	17.8	0.95	8.8	8.8
[O II] 7330	48.3	0.83	22.5	22.5
[O II] 7330	30.5	0.12	27.3	27.3

The fluxes, F, are normalized to $H\beta = 100$.

in the IRAF’s atomic data directory, are required. These atomic data were taken from Benjamin, Skillman & Smits (1999). Total chemical abundance derivation uses the ionic correction factors (ICF) formalism of Kingsburgh & Barlow (1994).

3.4 2D_NEB package: benchmarks

In this section we show the calculations that were performed to benchmark the results obtained from the 2D_NEB package. This was done by using arbitrary input data covering reasonable PN values, and the results of each step are checked by comparing them with the results given by the tasks of IRAF’s *nebular* package.

The first benchmark that we show concerns the performance of the extinction correction routine. As the *redcorr* task (`stdas.analysis.nebular`) works with the original coefficients from the Cardelli, Clayton & Mathis (1989) extinction function, we adapted our algorithm to also work with these coefficients. We performed the extinction correction using this extinction function and adopting $R_V = 3.1$, as is done in IRAF. We choose 4 different values for λ , well distributed inside the optical spectroscopic range. For each of these wavelengths, we choose different values of $c(H\beta)$ and non-corrected observed fluxes.

Table 4 presents the results of the extinction correction for the tested values. The values were used to generate 2D images that were then fed through 2D_NEB. Table columns are, respectively: line identification, observed flux, extinction coefficient and the extinction-corrected intensity given by the 2D_NEB (I_{2d_neb}) and by *redcorr* ($I_{redcorr}$). Note that the last two columns are essentially equal (with discrepancies always lower than 1%), indicating that our algorithm for deriving extinction corrections is working perfectly.

The next benchmark we performed concerns N_e and T_e determination. We choose to show the results for typical density and temperature diagnostics in photoionized nebulae, when only the optical spectra is available. For each of these quantities we show different values of assumed electron temperature or density, and different values for the diagnostic line ratios. The line ratios were chosen in a way to cover the range of possible values given in Osterbrock & Ferland 2006. T_e and N_e benchmarking results are shown in Table 5. In this table, columns 1 to 5 show, respectively: the

Table 5. T_e and N_e benchmarks.

Output	Input	Ratio	2D_NEb	<i>temden</i>	δ (%)
	N_e (cm^{-3})		T_e (K)	T_e (K)	
T_e [N II]	1,500	250.00	7,113.9	7,114.1	0.0
T_e [N II]	2,500	102.67	9,397.2	9,399.2	0.0
T_e [N II]	4,000	70.00	10,809.8	10,802.7	0.1
T_e [O II]	1,300	14.59	14,287.5	14,259.7	0.2
T_e [O II]	3,000	21.48	8,271.6	8,257.8	0.2
T_e [O II]	4,300	24.30	7,007.5	7,005.9	0.0
T_e [O III]	1,000	850.00	7,007.5	7,008.4	0.0
T_e [O III]	3,000	77.34	14,222.5	14,223.0	0.0
T_e [O III]	5,000	301.76	8,953.0	8,937.7	0.2
T_e [S II]	4,700	3.73	9,054.8	9,056.2	0.0
T_e [S II]	2,800	4.01	11,878.0	11,897.0	0.2
T_e [S II]	1,300	5.05	14,180.2	14,152.4	0.2
	T_e (K)		N_e (cm^{-3})	N_e (cm^{-3})	
N_e [O II]	7,000	1.90	1,667.9	1,667.0	0.1
N_e [O II]	9,000	1.48	1,014.7	1,014.4	0.0
N_e [O II]	15,000	2.68	6,036.2	6,034.2	0.0
N_e [S II]	7,500	0.74	1,654.9	1,655.3	0.0
N_e [S II]	10,000	0.87	1,030.8	1,029.3	0.1
N_e [S II]	13,500	0.59	4,997.2	4,993.7	0.1
N_e [Cl III]	7,000	0.91	3,289.2	3,290.5	0.0
N_e [Cl III]	12,000	0.84	4,777.5	4,776.7	0.0
N_e [Cl III]	11,000	1.15	1,380.8	1,379.4	0.1
N_e [Ar IV]	9,000	0.94	4,952.5	4,957.8	0.1
N_e [Ar IV]	10,500	1.17	2,165.0	2,164.1	0.0
N_e [Ar IV]	12,000	1.28	1,174.4	1,173.6	0.1

quantity (output) to be determined, the assumed T_e or N_e , the line ratio, and the results calculated using 2D_NEb as well as those obtained by *temden* (*stsdas.analysis.nebular* – IRAF). Inspection of Table 5 clearly shows the similarity between the two results, which can also be seen in the last column, which gives the discrepancies between the results from 2D_NEb and *temden*. The discrepancies are, in all cases, lower than 1%.

The last benchmark we show is related to ionic abundance determination. We choose 4 different ions, and their main wavelengths within the optical range, to show the functionality of our routines. For each ion, we assumed a fixed value of electron temperature and density. Table 6 shows the results of these benchmarks. The first to the sixth column shows, respectively: the ion for which the abundance will be derived with its wavelength in Å, the adopted electron density, the adopted electron temperature, and finally the ionic abundance (X/H^+) determined by 2D_NEb and by the *ionic* task (*stsdas.analysis.nebular*). The last column shows the discrepancies, which are always lower than 1%.

Some other aspects of the 2D_NEb performance were also tested, such as the determination of the $c(H\beta)$ map, the derivation of critical densities, emissivities and wavelengths of each transition, and the calculation of the total chemical abundance maps. For space reasons, we not show these benchmarks here.

As a last example of the accuracy of our IDL routines in 2D_NEb, we make sure that the determination of $c(H\beta)$

Table 6. Benchmarks of the ionic abundances. Intensities are normalized to $H\beta = 100$.

Ion / $\lambda(\text{\AA})$	I	2D_NEb ($\times 10^{-7}$)	<i>ionic</i> ($\times 10^{-7}$)	δ (%)
Input:	$N_e = 5,000 cm^{-3}$	$T_e = 13,000 K$		
N ⁺ 5755	2.36	90.96	91.03	0.1
N ⁺ 6548	76.01	247.7	247.8	0.0
N ⁺ 6584	235.43	260.2	260.2	0.0
Input:	$N_e = 2,000 cm^{-3}$	$T_e = 8,500 K$		
O ⁰ 6300	1.10	40.56	40.54	0.0
O ⁰ 6363	0.70	81.20	81.16	0.0
Input:	$N_e = 1,500 cm^{-3}$	$T_e = 13,000 K$		
O ⁺⁺ 4959	60.91	273.3	273.0	0.1
O ⁺⁺ 5007	112.77	175.4	175.2	0.1
Input:	$N_e = 5,000 cm^{-3}$	$T_e = 8,000 K$		
S ⁺ 6717	2.76	6.038	6.040	0.0
S ⁺ 6731	9.73	12.12	12.12	0.0

agrees with the formulation given in Osterbrock & Ferland (2006):

$$c(H\beta) = \frac{\log[F(\lambda)/F(H\beta)]_{teo} - \log[F(\lambda)/F(H\beta)]_{obs}}{f(\lambda) - f(H\beta)}, \quad (1)$$

where $[F(\lambda)/F(H\beta)]_{teo}$ is theoretical ratio of another Balmer line relative to $H\beta$, $[F(\lambda)/F(H\beta)]_{obs}$ is the equivalent observed fluxes ratio, and $f(\lambda)$ is the value of the extinction curve in a given λ . There is good agreement of the critical densities, emissivities and wavelengths, of each transition, with the results obtained from IRAF's *ionic* task (*stsdas.analysis.nebular*). The agreement is always equal to or better than 99%.

4 SLIT VERSUS SPECTROSCOPIC MAP RESULTS

In this section we show the results (electron densities, temperatures and ionic abundances) obtained from a single slit, and compare them with those obtained from the corresponding region of the spectroscopic maps. Following the same kind of comparison that we did in Section 3.2, slit G will be used. Table 7 lists the extinction-corrected intensities obtained from slit G, for the six nebular regions under analysis: north filament (NF), NOS, NIR, SIR, SOS and WN (see Table 2 for the definition of these structures). Table 8 lists the results obtained from these intensities (columns 2 to 8). The electron densities and temperatures adopted for the ionic abundance calculations were N_e [S II] and T_e [N II]. It was not possible to determine T_e and N_e for the NF. Because of this, the N_e [S II] and T_e [N II] values of the NES were adopted to enable the estimation of the ionic abundances of the NF region.

From the results of the slit G physical parameters (Table 8), one can notice the very low regional variation of the T_e [N II]. On the other hand, the spatial variation of the N_e [S II] is significant. These results should be compared with those coming from the same region of the spectroscopic

maps. The quantities shown with brackets in Table 8 are the corresponding mean values from the spectroscopic map for the region where the slit G was placed. As we were not able to calculate a $T_e[\text{O III}]$ map, the results of this parameter refer only to the slit G.

These results (those obtained directly from the slit and those obtained from the maps) are in agreement and, with the exception of the $N_e[\text{S II}]$ estimate of the NIR region (discrepancy of $\sim 21\%$), all of them show discrepancy of $\sim 10\%$ or less.

In particular, the spatial $N_e[\text{S II}]$ variation encountered in the analysis of the slit G, can be clearly visualized in the $N_e[\text{S II}]$ map (Figure 7). The absence of variation of $T_e[\text{N II}]$, from region to region, as shown by the slit G results, can also be visualized on the results obtained from the $T_e[\text{N II}]$ map. Note that the histogram of this map is much more concentrated around the mean value than the $N_e[\text{S II}]$ histogram.

5 MAPPING RESULTS

The 31 emission-line maps that were constructed using the spectroscopic mapping technique are listed in Table 1. The corresponding fluxes and intensities, of the entire nebula (WN), as well as the adopted SNR cut-off values (see Section 3.1) are also given in this table.

The emission-line map of $\text{H}\alpha$ was already shown in Figure 3. Other maps –namely: $\text{H}\beta$, $[\text{O III}]$ 5007 Å, $[\text{N II}]$ 6584 Å and $[\text{S II}]$ 6731 Å– are shown here, in Figure 5.

5.1 Extinction Correction

After creating the emission-line maps, we calculated the $c(\text{H}\beta)$ map using the 2D_{NEB} package. $\text{H}\alpha$, $\text{H}\gamma$ and $\text{H}\delta$ maps (weighted by their fluxes) and the Cardelli et al. (1989) extinction curve were all considered in deriving the $c(\text{H}\beta)$ map. The variation of $c(\text{H}\beta)$ across the nebula can be seen in Figure 6. The spectroscopic map clearly shows that $c(\text{H}\beta)$ is not constant throughout NGC 40, and the corresponding histogram shows its dispersion. The mean value computed from this map, which includes only valid values (of the pixels that survived the noise-mask cleaning) is 0.42. The spatial variation of $c(\text{H}\beta)$, seen in Figure 6, suggests that the amount of dust across the nebula is not constant and/or the dust grains have different characteristics from region to region (Spitzer 1998; Monteiro et al. 2005). Note that in studying a portion of the nebula Clegg et al. (1983) found $c(\text{H}\beta)=0.70$. In our map this region corresponds to an area where $c(\text{H}\beta)$ values are higher than average –with minimum and maximum values of ~ 0.22 and ~ 1.03 , respectively– whose median, 0.62, is in agreement with Clegg et al. (1983).

Pottasch et al. (2003) and Aller et al. (1972), using data from various regions of the nebula, found $c(\text{H}\beta)=0.605$ and $c(\text{H}\beta)=0.33$, respectively, both in reasonable agreement with our map. Studying a low-ionization region of the nebula (not clearly identified in their paper), Aller & Czyzak (1979) found $c(\text{H}\beta)=0.65$. And Liu et al. (2004a), analysing long-slit observations along the NGC 40 major axis found, similar to previous results, $c(\text{H}\beta)=0.70$. The previous results indicate that our mean value of $c(\text{H}\beta)$ lies in between the values found by other authors, who used data from different regions of NGC 40. Furthermore, as we have access to

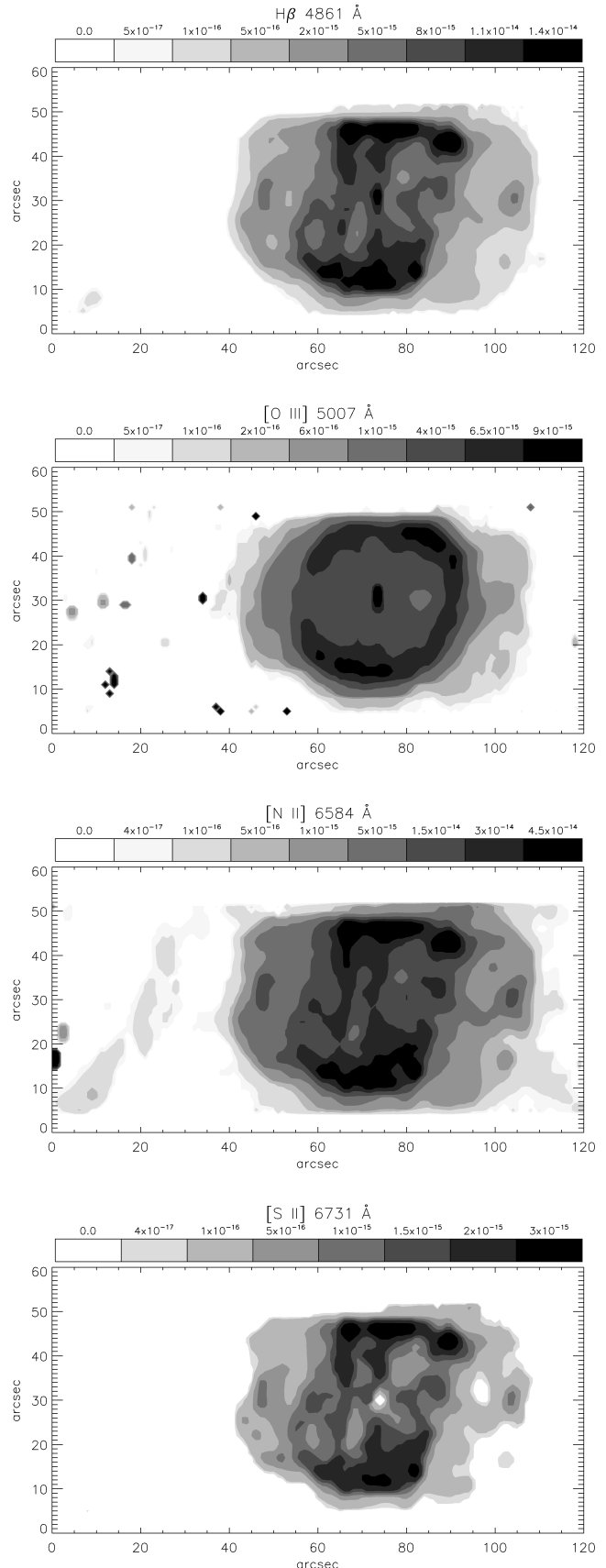


Figure 5. From the top to the bottom, the following emission-line maps (in $\text{erg cm}^{-2} \text{s}^{-1}$) are presented: $\text{H}\beta$, $[\text{O III}] \lambda 5007 \text{ \AA}$, $[\text{N II}] \lambda 6584 \text{ \AA}$ and $[\text{S II}] \lambda 6731 \text{ \AA}$.

Table 7. Emission-line intensities of slit G. For WN, whose emission was integrated along the slit, the observed flux is also given. Intensities and fluxes are normalized to $H\beta = 100$.

Line Identification	Slit Intensities						WN	
	NF	NS	NIR	SIR	SS	F	I	
$H\beta$ 4861 (erg cm ⁻² s ⁻¹)	8.13(-16)	2.21(-13)	8.18(-13)	9.38(-13)	2.05(-13)	2.67(-12)		
H10 3797	–	4.80	4.84	5.68	5.56	5.34	6.84	
He I 3820	–	–	0.85	1.86	–	3.11	3.97	
H9 3835	–	7.45	7.59	8.87	7.18	8.49	10.80	
[Ne III] 3869	–	–	1.05	–	–	1.19	1.50	
H8+He I 3888	–	15.51	17.85	21.57	15.8	22.94	28.90	
He I+[Ne III]+He I 3968	–	15.88	15.39	16.37	15.71	16.44	20.79	
[Fe III]+He I 4009	–	–	0.18	–	–	–	–	
He I 4026	–	–	1.49	1.17	–	1.39	1.70	
S II 4033	–	–	0.33	–	–	–	–	
[S II]+[S II] 4069+76	–	2.24	2.74	4.48	2.46	9.91	12.01	
H δ 4101	–	25.28	24.70	25.54	24.41	19.34	23.27	
H γ 4340	–	44.85	45.55	46.96	45.42	40.99	46.51	
[O III] 4363	–	–	0.70	0.90	–	2.66	3.00	
He I 4388	–	–	0.36	0.53	–	–	–	
He I 4438+?	–	–	–	1.09	–	9.49	10.49	
He I 4471	–	2.67	2.90	3.18	2.39	3.89	4.27	
N III 4524	–	–	–	0.18	–	–	–	
He II 4542	–	–	–	0.32	–	–	–	
Mg I 4563+71	–	1.01	0.51	0.58	0.75	–	–	
[C III]+[C IV] 4652	–	–	2.38	12.27	–	–	–	
He II 4686*	–	–	0.70	3.88	–	–	–	
[Ar IV] 4711	–	–	0.51	0.56	0.78	–	–	
$H\beta$ 4861	100.00	100.00	100.00	100.00	100.00	100.00	100.00	
He I 4921	–	–	1.20	1.43	0.89	1.71	1.69	
[O III] 4959	–	10.91	23.01	21.98	6.49	18.76	18.38	
[O III] 5007	–	33.14	68.98	66.25	19.2	57.1	55.39	
[N I] 5198+5200	–	1.37	0.92	0.93	1.34	0.33	0.31	
[Fe II]+[Fe III] 5262+70	–	–	0.41	0.46	–	1.4	1.29	
[Cl III] 5517	–	0.26	0.34	0.37	0.44	0.58	0.52	
[Cl III] 5537	–	0.28	0.37	0.32	0.47	0.56	0.50	
[O I] 5577	–	0.90	0.41	0.37	–	–	–	
[N II] 5755	–	2.97	2.92	2.99	2.92	3.51	3.02	
He I 5876	–	9.60	11.61	12.38	9.11	20.62	17.51	
? 5891	–	–	0.47	0.47	–	4.23	3.59	
[O I] 6300	–	5.47	3.73	3.48	5.11	4.78	3.87	
[S III]+He II 6312	–	0.54	0.74	0.69	0.23	1.03	0.83	
[O I] 6363	–	1.78	1.22	1.19	1.63	1.42	1.14	
He II 6406	–	–	0.12	–	–	1.16	0.93	
[N II] 6548	110.20	87.57	84.10	85.19	88.53	105.90	83.45	
H α 6563	310.62	296.92	296.43	300.18	298.7	377.43	296.95	
[N II] 6584	375.66	267.88	258.05	256.87	269.22	328.89	258.18	
He I 6678	–	3.04	3.24	3.59	2.96	4.00	3.11	
[S II] 6717	34.38	11.60	11.28	9.57	11.45	13.09	10.13	
[S II] 6731	18.42	15.03	15.34	13.47	13.66	20.77	16.05	

* The He II 4686 emission-line of SIR is probably blended with O II 4676 emission-line. We were not able to give a clear identification to the lines marked with “?”.

the spatial variation of $c(H\beta)$, it is clear why previous works found different extinction constants. The trend of deriving higher $c(H\beta)$ values in particular portions of the nebula is clearly identified in the map of Figure 6.

The $c(H\beta)$ map was used for extinction correction of the 31 emission-line maps. In this process, each pixel of each spectroscopic map had its extinction correction done based on the value of its corresponding pixel in the $c(H\beta)$ map. This procedure was performed by 2D_NEB.

After the extinction correction we calculated the mean intensities for each emission-line of NGC 40 by integrating

the emission of each spectroscopic map. These mean intensities were normalized to $H\beta = 100$ and are shown in the last column of Table 1, Section 3.1. Note that, as a consequence of using the $c(H\beta)$ map to correct each emission-line map, if a given line-map pixel has survived the noise-mask cleaning in its map, but has not survived this process in the $c(H\beta)$ map, then the pixel is not a valid pixel in the subsequent extinction-corrected emission-line map. As such the mean intensities, shown in the last column of Table 1, may not correspond to the same number of pixels as the mean fluxes (shown in the third column of the same table).

Table 8. Mean electron densities, temperatures and ionic abundances: slit G versus spectroscopic mapping results.

Parameter	Slit G results						Map results		Literature	
	NF	NS	NIR	SIR	SS	WN	Mean	Inf.L.	Pottasch ¹	Liu ²
$N_e[\text{S II}]$ (cm^{-3})	–	1,500 (1,350)	1,750 (2,250)	2,050 (2,200)	1,100 (1,150)	1,750 (1,850)	1,650	–	2,100	1,750
$T_e[\text{N II}]$ (K)	–	9,050 (8,550)	9,100 (8,800)	9,100 (8,750)	9,050 (8,850)	9,050 (8,800)	8,850	–	7,500	8,400
$T_e[\text{O III}]$ (K)	–	–	11,600	12,950	–	11,900	–	–	10,500	10,600
He^+/H^+ 4471	–	–	–	–	–	–	4.86(-2)	1.98(-2)	4.8(-2)	6.1(-2)
He^+/H^+ 5876	–	–	–	–	–	–	7.45(-2)	5.94(-2)	4.4(-2)	6.2(-2)
He^+/H^+ 6678	–	–	–	–	–	–	6.11(-2)	3.70(-2)	–	5.9(-2)
He^+/H^+ Mean	–	–	–	–	–	–	7.08(-2)	5.66(-2)	–	6.2(-2)
$\text{He}^{++}/\text{H}^+$ 4686	–	–	–	–	–	–	1.32(-3)	4.09(-5)	–	3.4(-5)
He/H	–	–	–	–	–	–	7.08(-2)	5.66(-2)	> 4.6(-2)	–
$\text{He}/\text{H}_{(ICF-P)}$	–	–	–	–	–	–	9.32(-2)	7.45(-2)	–	–
$\text{He}/\text{H}_{(ICF-L)}$	–	–	–	–	–	–	1.18(-1)	9.40(-2)	–	1.19(-1)
N^0/H^+ 5198+5200	–	1.81(-6)	1.35(-6)	1.41(-6)	1.77(-6)	3.69(-6)	–	–	–	–
N^+/H^+ 5755	–	6.95(-5)	6.65(-5)	6.61(-5)	6.98(-5)	6.57(-5)	7.32(-5)	4.52(-5)	–	–
N^+/H^+ 6548	8.53(-5)	6.77(-5)	6.46(-5)	6.50(-5)	6.83(-5)	6.46(-5)	6.92(-5)	6.90(-5)	–	7.58(-5)
N^+/H^+ 6583	9.86(-5)	7.02(-5)	6.72(-5)	6.64(-5)	7.04(-5)	6.73(-5)	7.05(-5)	7.05(-5)	1.01(-4)	–
N^+/H^+ Mean	9.56(-5)	6.96(-5)	6.65(-5)	6.60(-5)	6.99(-5)	6.66(-5)	7.05(-5)	7.04(-5)	–	–
O^0/H^+ 5577	–	1.53(-4)	6.83(-5)	6.00(-5)	–	6.71(-5)	–	–	–	–
O^0/H^+ 6300	–	1.56(-5)	1.05(-5)	9.63(-6)	1.46(-5)	1.11(-5)	9.98(-6)	6.37(-6)	–	–
O^0/H^+ 6363	–	1.59(-5)	1.07(-5)	1.02(-5)	1.46(-5)	1.25(-5)	1.03(-5)	3.99(-6)	–	–
O^0/H^+ Mean	–	2.95(-5)	1.45(-5)	1.31(-5)	1.46(-5)	1.49(-5)	1.02(-5)	6.51(-6)	–	–
O^{++}/H^+ 4363	–	–	7.43(-5)	9.28(-5)	–	7.14(-5)	–	–	–	–
O^{++}/H^+ 4959	–	1.58(-5)	3.29(-5)	3.10(-5)	9.44(-6)	2.87(-5)	3.55(-5)	3.12(-5)	–	1.20(-5)
O^{++}/H^+ 5007	–	1.56(-5)	3.42(-5)	3.24(-5)	9.69(-6)	3.00(-5)	3.21(-5)	3.08(-5)	1.9(-5)	–
O^{++}/H^+ Mean	–	1.57(-5)	3.41(-5)	3.25(-5)	9.63(-6)	3.00(-5)	3.43(-5)	3.31(-5)	–	–
O/H	–	4.51(-5)	4.86(-5)	4.56(-5)	2.43(-5)	4.49(-5)	4.10(-5)	3.97(-5)	5.3(-4)	8.83(-3)
$\text{Ne}^{++}/\text{H}^+$ 3869	–	–	1.75(-6)	–	–	1.68(-6)	–	–	8.3(-7)	5.33(-7)
S^+/H^+ 4069	–	8.21(-7)	–	–	9.76(-7)	3.63(-6)	–	–	–	1.17(-6)
S^+/H^+ 6717	2.99(-6)	1.01(-6)	1.03(-6)	9.21(-7)	9.01(-7)	9.86(-7)	8.88(-7)	7.63(-7)	–	1.24(-6)
S^+/H^+ 6731	1.24(-6)	1.01(-6)	1.04(-6)	9.20(-7)	9.03(-7)	9.90(-7)	8.83(-7)	7.53(-7)	1.48(-6)	–
S^+/H^+ Mean	2.38(-6)	1.00(-6)	1.03(-6)	9.21(-7)	9.02(-7)	1.18(-6)	8.85(-7)	7.74(-7)	–	–
S^{++}/H^+ 6312	–	2.01(-6)	2.70(-6)	2.47(-6)	8.66(-7)	2.69(-6)	–	–	2.8(-6)	1.34(-6)
$\text{Cl}^{++}/\text{H}^+$ 5517	–	4.38(-8)	5.79(-8)	6.37(-8)	7.17(-8)	5.18(-8)	1.02(-7)	1.88(-8)	5.9(-8)	4.19(-8)
$\text{Cl}^{++}/\text{H}^+$ 5537	–	5.31(-8)	6.87(-8)	5.82(-8)	9.11(-8)	5.28(-8)	4.04(-7)	1.86(-7)	7.5(-8)	–
$\text{Cl}^{++}/\text{H}^+$ Mean	–	4.87(-8)	6.35(-8)	6.12(-8)	8.16(-8)	5.23(-8)	3.99(-7)	1.91(-7)	–	–
$\text{Ar}^{+3}/\text{H}^+$ 4711	–	–	1.15(-7)	1.27(-7)	1.74(-7)	1.22(-7)	3.92(-7)	4.94(-8)	–	–

Pottasch¹: Pottasch et al. (2003).Liu²: Liu et al. (2004a,b).

*The central star was not considered in the determination of the physical and chemical parameters of whole nebula, WN.

5.2 N_e and T_e Physical Properties

Using the 2D_{NEB} the $T_e[\text{N II}]$ and $N_e[\text{S II}]$ maps were calculated. For $N_e[\text{S II}]$, we first assumed a constant electron temperature, equal to 9,000 K, throughout the map. The resultant map was subsequently used to calculate the $T_e[\text{N II}]$ map, and then the $N_e[\text{S II}]$ was recalculated using this $T_e[\text{N II}]$ map.

The region with valid pixels in the $T_e[\text{N II}]$ map was limited by the noise-mask cleaning of the $[\text{N II}]$ 5755 Å emission-

line map. As the determination of $N_e[\text{S II}]$ depends on the electron temperature, we assumed a constant temperature equal to 9,000 K for the non-valid pixels of the $T_e[\text{N II}]$ map. $T_e[\text{N II}]$ and $N_e[\text{S II}]$ maps are shown in Figure 7. In the $N_e[\text{S II}]$ map, the dashed line indicates the outer limit between the region in which $N_e[\text{S II}]$ has been calculated by adopting $T_e[\text{N II}] = 9,000$ K, and the region in which the $T_e[\text{N II}]$ map was used.

The mean values of $T_e[\text{N II}]$ and $N_e[\text{S II}]$ are, respectively, 8,850 K and $1,650 \text{ cm}^{-3}$. Comparing with the liter-

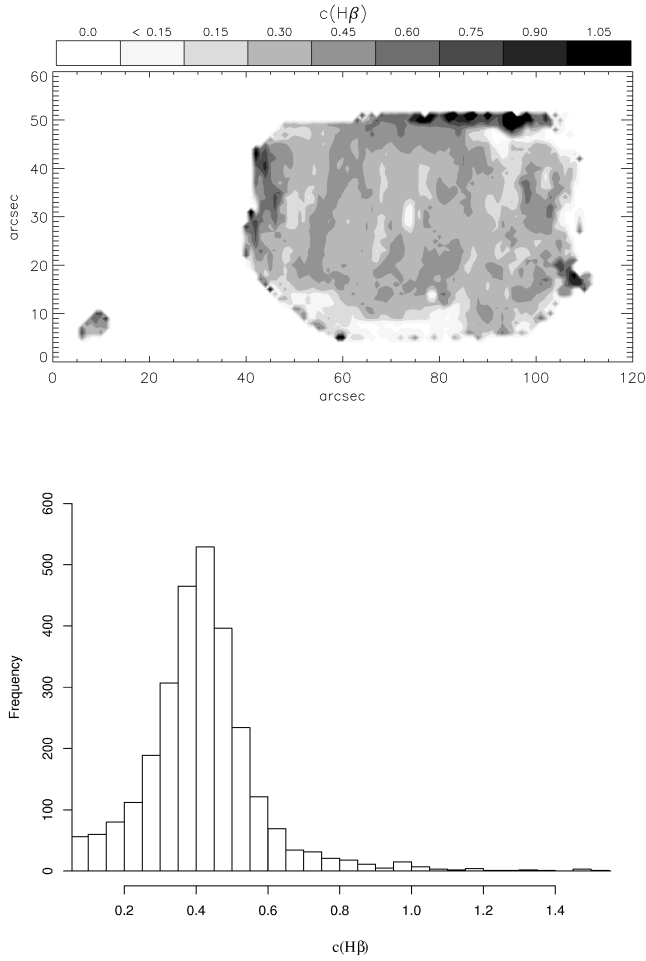


Figure 6. Top: $c(\text{H}\beta)$ map of NGC 40. Bottom: The histogram from the $c(\text{H}\beta)$ map. The mean value of the $c(\text{H}\beta)$ map is 0.42.

ature (Table 8; columns 10 and 11), the mean values we found for $N_e[\text{S II}]$ and $T_e[\text{N II}]$ are marginally in agreement with previous determinations of the physical properties in NGC 40. Notice that the $N_e[\text{S II}]$ value determined by Pottasch et al. (2003) ($2,100 \text{ cm}^{-3}$) is very similar to the values that we found for the NIR and SIR regions, when we used the data from the slit G (and from the $N_e[\text{S II}]$ map, at that same region). On the other hand, one can notice that the $N_e[\text{S II}]$ map shows great variations, even if we consider the internal region only. The values found by Liu et al. (2004a) ($1,750 \text{ cm}^{-3}$) and by Delgado-Inglada et al. (2009) ($1,800 \text{ cm}^{-3}$) approach our mean $N_e[\text{S II}]$ map result. They both used the same line intensities. The $T_e[\text{N II}]$ results from Liu et al. (2004a) (8,400 K) and Delgado-Inglada et al. (2009) (8,600 K) again are closer to the mean value of the $T_e[\text{N II}]$ map than the one found by Pottasch et al. (2003). Actually, when we look at the $T_e[\text{N II}]$ map, we hardly see any region with values as low as that found by Pottasch et al. (2003) (7,500 K), and most of the nebula shows $T_e[\text{N II}] > 8,000 \text{ K}$.

It was not possible to calculate the $T_e[\text{O III}]$ spectroscopic map due to the very faint emission of $[\text{O III}] 4363 \text{ \AA}$.

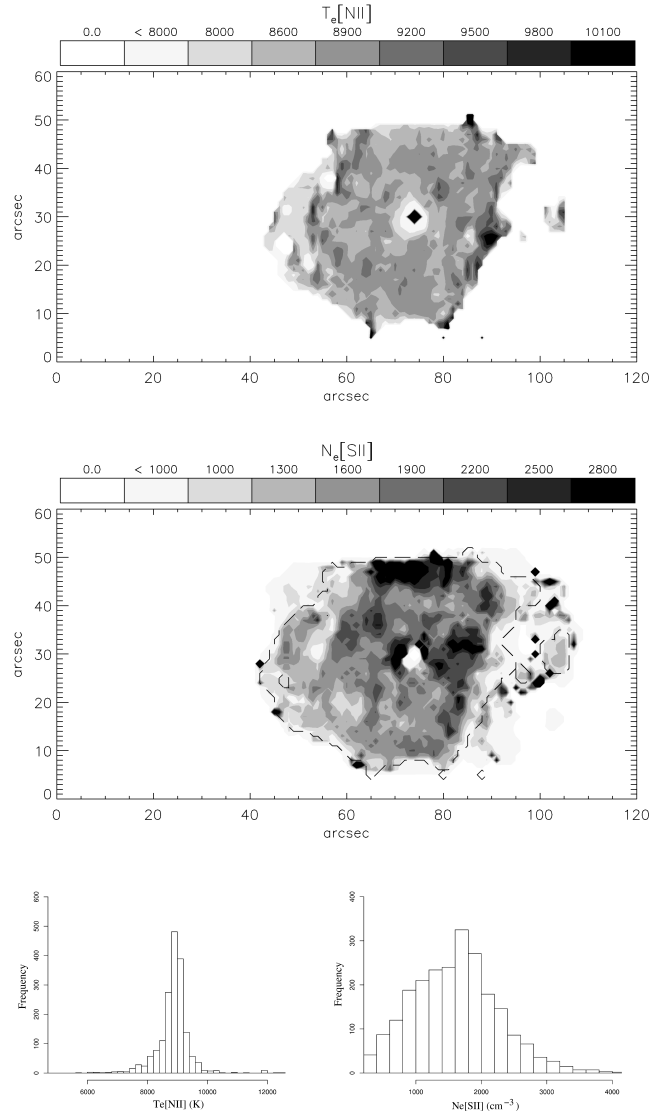


Figure 7. From the top to the bottom, the following NGC 40 physical properties plots are shown: $T_e[\text{N II}]$ map, (in K), $N_e[\text{S II}]$ map (in cm^{-3}), $T_e[\text{N II}]$ histogram and $N_e[\text{S II}]$ histogram. The region inside the dashed line, on the $N_e[\text{S II}]$ map, was calculated adopting the electronic temperature from the $T_e[\text{N II}]$ map. A temperature equal of 9,000 K has been adopted for the outer region.

In cases like this, the usual analysis made using a single slit has an advantage since the emission is integrated throughout a region, or throughout the whole nebula, thus the very faint emission-line flux is improved in signal to noise. This procedure may allow the calculation $T_e[\text{O III}]$. In fact, in the case of NGC 40, we did derive $T_e[\text{O III}]$ in two nebular regions (NIR and SIR) using the fluxes of slit G, as shown in Table 8.

5.3 Ionic and Total Chemical Abundances

$T_e[\text{N II}]$ and $N_e[\text{S II}]$ maps were used to calculate the ionic abundance maps. For the non-valid pixels of these

maps we assumed constant values, $T_e = 9,000$ K and $N_e = 1,600 \text{ cm}^{-3}$. When more than one emission-line was available for determining the ionic abundance of a certain ion, all the strong lines were used, each resulting in an independent ionic abundance map. Then, the ionic abundance map was generated from these individual maps weighted by intensity. These are the ionic maps shown in Figure 8 and Figure 9.

The mean values of the ionic abundances are listed in Table 8, in the first column of the map results. We draw attention to the fact that these mean values were calculated only over the pixels that have survived the noise-mask cleaning. This means that the abundance maps which have non-valid pixels inside the nebular regions would have, in reality, lower mean abundances if the entire nebula were considered.

As an attempt to determine the abundances representative of the whole nebula (WN, in the tables) for the cases that have non-valid pixels inside the nebular region, we calculated, for each abundance map, the sum of the ionic abundances of all pixels and divided the result by the number of pixels that compose the nebula¹. These results represent the lower limits of the corresponding NGC 40 abundances. These lower limits (Inf.L.) are also shown in Table 8, column 9.

The mean ionic abundances determined in this paper can be compared with the results found in the literature, by inspecting Table 8. For some cases the lower limit (column 9) is closer to the previous ionic determinations. That is obvious for $\text{He}^{++}/\text{H}^+$ $\lambda 4686$ abundance, whose map shows almost no presence of that specie. The ionic abundances from $\text{Cl}^{++}/\text{H}^+$ $\lambda 5517$, $\text{Cl}^{++}/\text{H}^+$ $\lambda 5537$, N^+/H^+ $\lambda 6583$, O^{++}/H^+ $\lambda 4959$, O^{++}/H^+ $\lambda 5007$, S^+/H^+ $\lambda 6717$ and S^+/H^+ $\lambda 6731$ show a somewhat different result when compared with the literature. The discrepancies vary from 70% up to a factor of 3. These discrepancies can be due to the fact that here, we are analysing a bigger area of the object: the whole nebula, instead of one long slit, as in the case of Liu et al. (2004a), and a set of small portions, in the case of Pottasch et al. (2003)). Notice, for instance, that despite the fact that the mean value of our $\text{Cl}^{++}/\text{H}^+$ map (3.99×10^{-7}) is higher than the mean value from Liu et al. (2004a) (4.19×10^{-8}) and Pottasch et al. (2003) (5.9×10^{-8} and 7.5×10^{-8}), the inner rim presents a lower $\text{Cl}^{++}/\text{H}^+$ abundance when compared to the shell (see Figure 8). The result we found for the inner rim is closer to the results from the literature.

Examining the ionic distributions of O^0/H^+ , N^+/H^+ , S^+/H^+ , He^+/H^+ and that of O^{++}/H^+ , in Figure 8 and Figure 9, we see a region (a diagonal, from left to right, that includes the location of the central star) in which ionic fractions coming from the low-ionization species (O^+/H^+ , N^+/H^+ and S^+/H^+) are less abundant when contrasted with the neighbor-nebular portions. On the other hand, the map of O^{++}/H^+ and He^+/H^+ show values higher than the average at the same region. It is worth noticing that, even though He^+/H^+ is a low-ionization specie, a great amount of

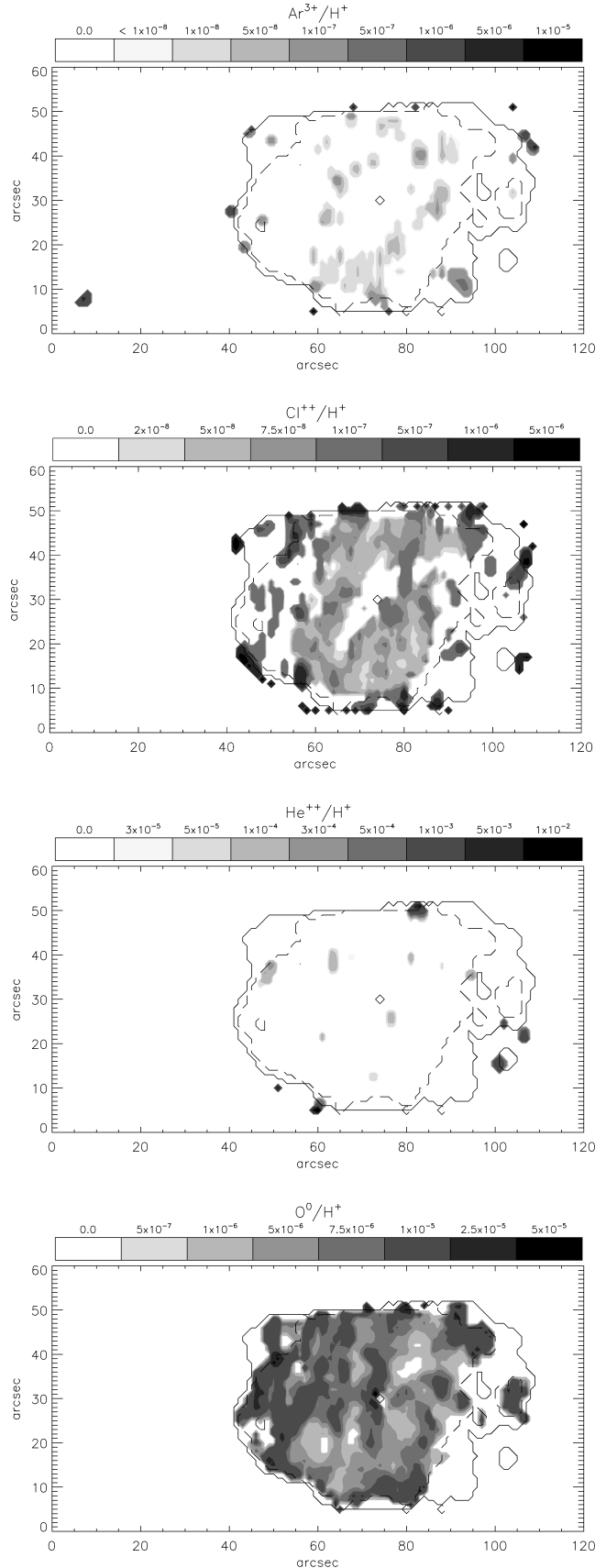


Figure 8. From the top to the bottom, the following ionic abundance maps are presented: Ar IV, Cl III, He II and O I.

¹ Since all abundance maps are restricted by the locations where the $c(\text{H}\beta)$ map is valid, we used the number of valid pixels of the $c(\text{H}\beta)$ map for the number of pixels that compose the nebula

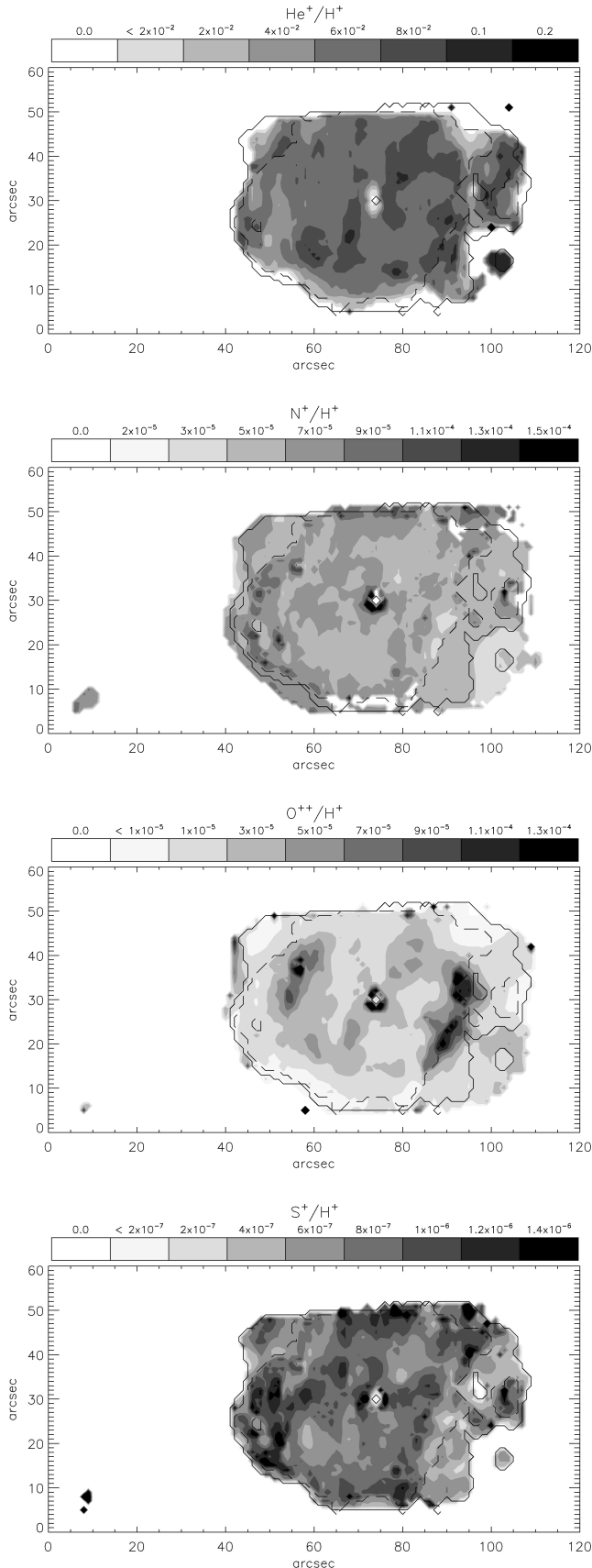


Figure 9. From the top to the bottom, the following ionic abundance maps are presented: He I, N II, O III and S II.

He^0 is also expected to be present in this low ionization nebula. In spite of the peculiar behaviour of the low-ionization ions, as well as O^{++}/H^+ and He^+/H^+ , the electron temperature maps (particularly relevant for abundance determinations) have no obvious gradient (see corresponding map in Figure 7) that would justify this result.

Is this higher ionization tunnel of emission in NGC 40 similar to the jet structures of a number of other nebulae? In NGC 7009, for instance, two pairs of low-ionization knots are clearly seen, in addition to a pair of jets, in which the excitation degree is significantly higher than that of the immediate vicinity (Gonçalves et al. 2003). However, contrary to what we find for NGC 40, in the case of NGC 7009 the electron density of the higher-ionization emission tunnel is a factor of 2 lower than in the other nebular regions. But note that in both cases the T_e is roughly the same throughout the nebula.

Concerning the element abundances of helium in NGC 40, He/H , we found the mean value of 7.08×10^{-2} . This result has been obtained by summing the He^+ and He^{++} ionic abundance maps, and taking its mean value. This extremely low total helium abundance can be explained by the fact that a significant amount of He^0 is expected to be present in a low excitation nebula like NGC 40, and He^0 was not considered in the He/H given above. To circumvent this kind of problem, Zhang & Liu (2003) suggested that an ICF based on the S^+ and S^{++} abundances can be used to account for the He^0 abundance of low excitation PNe. Using our own data we were not able to calculate a S^{++} abundance map, nevertheless, if we consider the S^{++} abundances found by Pottasch et al. (2003) and Liu et al. (2004b) (Table 8), and the mean value of the S^+/H^+ map that we calculated (8.88×10^{-7} , in Table 8), we can determine a more reliable value for the He total abundance of NGC 40. Doing this exercise, we find $\text{He}/\text{H}_{(\text{ICF-P})} = 9.32 \times 10^{-2}$, adopting S^{++}/H^+ from Pottasch et al. (2003), and $\text{He}/\text{H}_{(\text{ICF-L})} = 1.18 \times 10^{-1}$ by using S^{++}/H^+ from Liu et al. (2004b). These three He/H are shown in Table 8. Notice that the interval of S^{++} abundances from Pottasch et al. (2003) and Liu et al. (2004b) contains the mean S^{++} abundance we found from our slit G, if we consider the NS, NIR, SIR and SS regions (again, that is not the case for the WN region, because of the contamination from the central star region). And, finally, not only we believe that 9.32×10^{-2} and 1.18×10^{-1} should correspond to the lower and upper He abundance limits of NGC 40, but they are also similar to the previous results found by Liu et al. (2004b), who adopted the same ICF scheme to account for the unobserved amount of He^0 in the total helium abundance of NGC 40.

The total oxygen abundance map is shown in Figure 10. This map has been obtained summing the ionic abundance maps of O^0 and O^{++} –since, unfortunately, O^+ map is not available. This element abundance is, in fact, only a lower limit. The corresponding mean value of the O/H map is 4.10×10^{-5} ; a much lower value when compared with the results from the literature. That is a consequence of the absence of the O^+ abundance map. As shown by Pottasch et al. (2003) and Liu et al. (2004b), this ion dominates the oxygen abundance of this nebula.

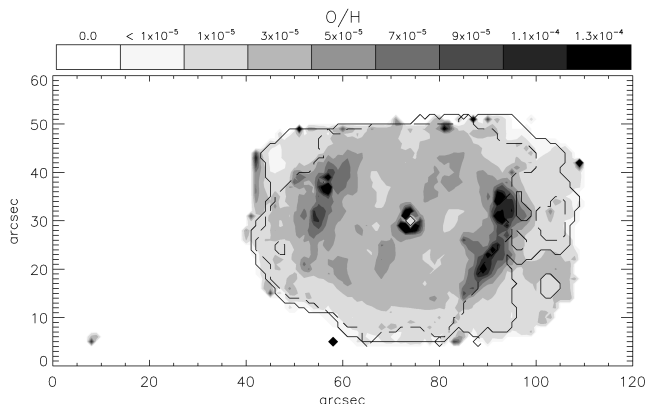


Figure 10. Inferior limit of the oxygen chemical abundance map.

6 SUMMARY AND CONCLUSIONS

In this paper we presented a spatially-resolved analysis of the physical and chemical characteristics of the planetary nebula NGC 40. To reach these results, 16 long-slit parallel optical spectra were obtained, from which we created 31 emission-line spectroscopic maps. These maps provide the spatially-resolved characteristics of the line emission, and the total fluxes for the whole nebula.

Using the usual diagnostic ratios, these maps were applied to calculate the 2D density, temperature and abundance information for this nebula. To derive these quantities, we adapted the tasks from the well-established IRAF *nebular* package (De Robertis et al. 1987), to work with two-dimensional data, thereby developing, and proving the efficiency of, the 2D_NEb package.

Each emission-line map was corrected for reddening, pixel by pixel, using the $c(\text{H}\beta)$ map that was created from the $\text{H}\alpha/\text{H}\beta$, $\text{H}\gamma/\text{H}\beta$ and $\text{H}\delta/\text{H}\beta$ map ratios. The $c(\text{H}\beta)$ map shows interesting features, with values that vary from less than ~ 0.2 up to more than ~ 0.6 , as shown in the histogram of Figure 6, with a mean characteristic of the whole nebula, $c(\text{H}\beta)$ equal to 0.42. The above spatial extinction variation could indicate that dust is mixed with the ionized gas of NGC 40.

Our $T_e[\text{N II}]$ map shows only a slight variation from region to region, from $\sim 8,000$ K up to $\sim 9,500$ K. On the other hand, these variations are much less prominent than those found in the $N_e[\text{S II}]$ map, where the values varies between $\sim 1,000 \text{ cm}^{-3}$ and $\sim 3,000 \text{ cm}^{-3}$. The histograms of both physical parameters, $T_e[\text{N II}]$ and $N_e[\text{S II}]$, show this dispersion. The density map also shows that there is a trend to lower density regions on the west side of the nebula, but it does not show any trend for the outer regions compared to the inner ones. The mean $N_e[\text{S II}]$ ($1,650 \text{ cm}^{-3}$) and $T_e[\text{N II}]$ ($8,850$ K), from the spectroscopic maps, are in good agreement with other results from the literature (Delgado-Inglada et al. 2009; Liu et al. 2004a; Pottasch et al. 2003; Clegg et al. 1983; Aller et al. 1972). On the other hand, the maps show spatial variations that were not addressed by previous works.

Several of the ionic abundance maps show significant spatial variations. i) The $\text{Ar}^{3+}/\text{H}^+$ and $\text{Cl}^{++}/\text{H}^+$ maps show

a ring structure on the inner region of NGC 40, and also high concentrations from these species on the outer region of the nebula. ii) The O^0/H^+ e O^{++}/H^+ maps show strong spatial variations. In the first case, the contrast of the regions with $\text{O}^0/\text{H}^+ < 10^{-5}$ is clear. For the second, most of the nebula has O^{++}/H^+ between 10^{-5} and 3×10^{-5} . However, regions with lower O^{++} abundances are present in the outer regions of the nebula, and regions in which O^{++}/H^+ varies from $\sim 5 \times 10^{-5}$ up to $\sim 1.3 \times 10^{-4}$ are found, primarily between the inner rim and outer shell. iii) The He^+/H^+ abundance is also inhomogeneous. iv) The N^+/H^+ abundance map shows that almost the whole nebula has an N^+/H^+ between 5×10^{-5} and 9×10^{-5} or that N^+/H^+ does not vary significantly throughout the nebula. v) Finally, the S^+/H^+ map shows clumps, in which the S^+/H^+ varies between less than 4×10^{-7} up to more than 10^{-6} .

It is important to point out that maps represent a projection of the nebula along the line of sight on the sky, and so nothing can be said about the tridimensional state of the gas (T_e , N_e , ionic as well as total abundances) from our analysis of NGC40.

However, the results obtained in this work allow us to conclude that the spatial variations found in the $c(\text{H}\beta)$, $T_e[\text{N II}]$, $N_e[\text{S II}]$, and abundance maps unequivocally confirm the necessity of an analysis with spatial resolution for a more complete study of the physical and chemical properties of planetary nebulae. Furthermore, the spectroscopic mapping technique used in this paper and in previous works shows important advantages when compared with the usual technique that uses one or a few long-slits to analyse the object. As an extra ingredient in this discussion, we note that Corradi et al. (1997), Perinotto & Corradi (1998), and Gonçalves et al. (2003, 2006) did not find significant spatial variation of the chemical abundances when analysing a number of other PNe. As we do find these variations in NGC 40, an important question that remains to be addressed is: if analysed with the spectroscopic mapping technique, as in this work, would those ~ 20 PNe studied with single long-slit spatially resolved spectra (above references) show significant chemical variations?

Also in the context of distant extragalactic PNe, it is clear that spatially resolved data using techniques similar to the one applied here to study NGC 40 are desirable. However, our telescopes/instruments prevent us of such a detailed study of distant objects. Fortunately in these situations most of the emission of a PN is captured in a single slit observation –making the average values more representative. And, therefore, the interpretation of results for distant extragalactic PNe are, at least in a statistical sense, not as seriously affected by the lack of spatial resolution.

ACKNOWLEDGMENTS

We would like to dedicate this paper to the memory of Hugo E. Schwarz, the observer of the data used here. We also thank John Danziger, the referee, for his revision of the paper with suggestions that helped to improved it. Three Brazilian agencies gave us partial support for this work. So MLLF, DRG and HM would like to thank CAPES, FAPERJ's E-26/110.107/2008 grant and FAPESP (2003/09692-0 grant), respectively.

REFERENCES

- Aller L., Czyzak S., Buerger E., et al., 1972, ApJ, 172, 361
 Aller L., Czyzak S., 1979, Ap&SS, 62, 397
 Balick B., Owen R., Bignell C. R., Hjellming R. M., 1987, AJ, 94, 948
 Balick B., Perinotto M., Maccioni A., Terzian Y., Hajian A., 1994, ApJ, 424, 800
 Benjamin R., Skillman E., Smits D., 1999, ApJ, 514, 307
 Bianchi L., Grewing M., 1987, A&A, 181, 85
 Cardelli J., Clayton G., Mathis J., 1989, ApJ, 345, 245
 Chiappini C., Romano D., Matteucci F., 2003, MNRAS, 339, 63
 Clegg R., Seaton M., Peimbert M., Torres-Peimbert S., 1983, MNRAS, 205, 417
 Corradi R. L. M., Perinotto M., Schwarz H. E., Claeskens J.-F., 1997, A&A, 322, 975
 De Robertis M., Dufour J., Hunt R., 1987, JRASC, 81, 195
 Delgado-Inglada G., Rodriguez M., Mampaso A. and Vironen K., 2009, ApJ, 694, 1335
 Feibelman W., 1999, ApJ, 514, 296
 Filippenko A. V., 1982, PASP, 94, 715
 Gonçalves D., Corradi R. L. M., Mampaso A., Perinotto M., 2003, ApJ, 597, 975
 Gonçalves D. R., Ercolano B., Carnero A., Mampaso A., Corradi R. L. M., MNRAS, 2006, 365, 1039
 Guerrero M. A., Manchado A., Serra-Ricart M., ApJ, 1996, 456, 651
 van den Hoek L. B., Groenewegen M. A. T., 1997, A&ASS, 123, 305
 Kingsburgh R., Barlow M. 1994, MNRAS, 271, 257
 Liu Y., Liu X.-W., Luo S.-G., Barlow M., 2004a, MNRAS, 353, 1231-1250
 Liu Y., Liu X.-W., Barlow M., Luo S.-G., 2004b, MNRAS, 353, 1251-1285
 Marigo P., 2001, A&A, 370, 194
 Monteiro H., Schwarz H., Gruenwald R., Heathcote S., 2004, ApJ 609, 194
 Monteiro H., Schwarz H., Gruenwald R., Guenthner K., Heathcote S., 2005, ApJ, 620, 321.
 Montez R. Jr., Kastner J. H., de Marco O., Soker N., 2005, ApJ 635, 381
 Morisset, C., & Georgiev, L. 2009, A&A, 507, 1517
 Mateluna-Perez R., Monteiro H., Richards J., Schwarz H., 2006, BAAS, 38, 1113
 O'Donnell J., 1994, ApJ, 422, 158
 Osterbrock D., Ferland G., 2006, *Astrophysics of Gaseous Nebulae and Active Galactic Nuclei*, University Science Books
 Peimbert M., 1978, IAUS, 76, 215
 Perinotto M., Corradi R. L. M., 1998, A&A, 332, 721
 Pottasch S., Bernard-Salas J., Beintema D., Feibelman W., 2003, A&A, 409, 599
 Quireza C., Rocha-Pinto H. J., Maciel W. J., 2007, A&A, 475, 217
 Ren D., Allington-Smith J., 2002, PASP, 114, 866
 Rice M., Schwarz H., Monteiro H., 2004, BAAS, 36, 1572
 Seaton M., 1979, MNRAS, 187, 73
 Schwarz, H. E., & Monteiro, H. 2006, ApJ, 648, 430
 Spitzer L., 1998, *Physical Processes in the Interstellar Medium*, Wiley-Interscience
 Stankevich K.S, Sharova O.I., 1983, SvA, 27, 537
 Tsamis Y. G., Walsh J. R., Péquignot D., Barlow M. J., Danziger I. J., Liu, X.-W., 2008, MNRAS, 386, 22
 Yin J., Magrini L., Matteucci F., Lanfranchi G. A., Gonçalves D. R., Costa R. D. D., 2010, A&A in press, A&A preprint doi <http://dx.doi.org/10.1051/0004-6361/201014377>
 Zhang Y., Liu X. -W., 2003, A&A, 404, 545

This paper has been typeset from a \TeX / \LaTeX file prepared by the author.